Mechanically Guided Hierarchical Assembly of 3D Mesostructures

Hangbo Zhao, Xu Cheng, Changsheng Wu, Tzu-Li Liu, Qinai Zhao, Shuo Li, Xinchen Ni, Shenglian Yao, Mengdi Han, Yonggang Huang,* Yihui Zhang,* and John A. Rogers*

3D, hierarchical micro/nanostructures formed with advanced functional materials are of growing interest due to their broad potential utility in electronics, robotics, battery technology, and biomedical engineering. Among various strategies in 3D micro/nanofabrication, a set of methods based on compressive buckling offers wide-ranging material compatibility, fabrication scalability, and precise process control. Previously reports on this type of approach rely on a single, planar prestretched elastomeric platform to transform thin-film precursors with 2D layouts into 3D architectures. The simple planar configuration of bonding sites between these precursors and their assembly substrates prevents the realization of certain types of complex 3D geometries. In this paper, a set of hierarchical assembly concepts is reported that leverage multiple layers of prestretched elastomeric substrates to induce not only compressive buckling of 2D precursors bonded to them but also of themselves, thereby creating 3D mesostructures mounted at multiple levels of 3D frameworks with complex, elaborate configurations. Control over strains used in these processes provides reversible access to multiple different 3D layouts in a given structure. Examples to demonstrate these ideas through both experimental and computational results span vertically aligned helices to closed 3D cages, selected for their relevance to 3D conformal biointerfaces and multifunctional microsystems.

1. Introduction

3D mesoscale structures with complex, hierarchical geometries are ubiquitous in nature. Such architectures support essential functions in both plant and animal life, such as flower stamens and petals for pollination, gecko's feet for controlled adhesion, and shark scales for drag reduction. These and other examples of 3D systems in living organisms also provide inspiration for engineered counterparts in electronics,[1–5] photonics,[6–9] biosensing,[10–13] energy storage systems,[14–17] mechanical and optical metamaterials,[18–23] microrobotics,[24–29] and other areas. Schemes for fabricating such structures focus on direct top-down or bottom-up techniques.[30–33] Although these methods have great utility, most also have some limitations in materials compatibility, geometric complexity, and design versatility. For instance, 3D printing techniques offer high structural resolution and topological flexibility, but they are not applicable to device-grade semiconductor materials. Alternative

H. Zhao, C. Wu, T.-L. Liu, S. Li, X. Ni, S. Yao, M. Han, Y. Huang,
J. A. Rogers
Querrey Simpson Institute for Bioelectronics
Northwestern University
Evanston, IL 60208, USA
E-mail: y-huang@northwestern.edu; jrogers@northwestern.edu

H. Zhao, Q. Zhao
Department of Aerospace and Mechanical Engineering
University of Southern California
Los Angeles, CA 90089, USA

X. Cheng, Y. Zhang
Applied Mechanics Laboratory
Department of Engineering Mechanics
Center for Flexible Electronics Technology
Tsinghua University
Beijing 100084, China
E-mail: yihuizhang@tsinghua.edu.cn

T.-L. Liu, Y. Huang, J. A. Rogers
Department of Mechanical Engineering
Northwestern University
Evanston, IL 60208, USA

S. Yao
Beijing Advanced Innovation Center for Materials Genome Engineering
School of Materials Science and Engineering
University of Science and Technology Beijing
Beijing 100083, China

M. Han
Department of Biomedical Engineering
College of Future Technology
Peking University
Beijing 100871, China

Y. Huang, J. A. Rogers
Department of Materials Science and Engineering
Northwestern University
Evanston, IL 60208, USA

Y. Huang, J. A. Rogers
Department of Civil and Environmental Engineering
Northwestern University
Evanston, IL 60208, USA

J. A. Rogers
Department of Biomedical Engineering
Northwestern University
Evanston, IL 60208, USA

**ADVANCED
SCIENCE NEWS**
www.advancedsciencenews.com

**ADVANCED
MATERIALS**
www.advmat.de

schemes rely on controlled mechanical buckling to transform patterned 2D structures (referred to as 2D precursors) of desired materials, sometimes in the form of completed planar devices, into targeted 3D mesostructures.[34–38] Such methods are intrinsically compatible with the most sophisticated planar microfabrication technologies, and they apply naturally to wide-ranging types of advanced materials including metals, device-grade semiconductors, and functional polymers with critical dimensions from the nanoscale to macroscale. Various control parameters and design strategies provide routes to diverse 3D topologies, including origami- and kirigami-inspired designs,[36,39,40] in multilayered configurations,[41] with dissolvable components,[42] across nonuniform substrates for assembly,[43] with chiral features,[44] and in layouts that can be transformed in a reversible fashion to realize multiple operating modes[45–48] and high packing ratios.[49] One limitation, however, is that the simple planar elastomeric substrates used to initiate the assembly process can constrain the types of 3D geometries that can be achieved. Specifically, 3D mesostructures with base regions that distribute throughout a 3D space, those with multiple levels of 3D features in hierarchical configurations, and fully closed cage structures are not possible.

Here we report concepts that exploit complex, 3D elastomeric substrates, as alternatives to those with simple, planar geometries. Multiple layers of 2D precursors bonded to such substrates, each stretched to different levels of prestrain separately and adhered at selected locations, yield a controlled sequence of compressive buckling motions of both the substrates and non-elastomeric 2D precursors. This scheme enables assembly of qualitatively different classes of 3D mesostructures compared to those reported previously, including 3D ribbons, membranes and meshes on top of 3D frameworks, 3D helices across different levels of supporting structures, and mesoscale cages that can morph between half-open to fully closed states. The levels of geometric complexity in these and other cases cannot be achieved with a single assembly substrate or a set of planar bonding sites. Experimental and theoretical studies of nearly two dozen 3D mesostructures demonstrate some of the types of hierarchical structures that are uniquely enabled by these ideas.

2. Results and Discussion

2.1. Basic Hierarchical Assembly Process

Figure 1a presents a schematic illustration of the approach, along with quantitative comparisons of experimentally realized

J. A. Rogers
Department of Chemistry
Northwestern University
Evanston, IL 60208, USA

J. A. Rogers
Department of Neurological Surgery
Northwestern University
Evanston, IL 60208, USA

J. A. Rogers
Department of Electrical and Computer Engineering
Northwestern University
Evanston, IL 60208, USA

and computationally predicted geometries of a basic, representative 3D mesostructure formed by this hierarchical assembly process. The scheme starts with the preparation of two layers of independently prestretched elastomeric substrates (Dragon Skin, Smooth-On) bonded at selected locations. Here, stretching a patterned, top elastomeric substrate (approximately 200 μm in thickness) to a biaxial strain of 50%, stretching a separate, unpatterned bottom substrate (approximately 2 mm in thickness) of the same material to a biaxial strain 100%, and then bonding them at selected locations (referred to as bonding sites on the top substrate) prepares the base structure that will initiate the process of 3D transformation. Details appear in Figure S1, Supporting Information, and the Experimental Section. The next step involves laminating a 2D precursor of polyimide (PI; 4 μm in thickness and 150 μm in width) onto this prestretched bilayer substrate at selected bonding sites. Details appear in Figure S2, Supporting Information, and the Experimental Section. In this basic design, four bonding sites on the 2D precursor ribbon align with one line of the cross-shaped top substrate. Releasing the prestrain of the bottom substrate initiates a two-stage, 2D to 3D shape transformation of this trilayer assembly. During the first stage (Stage I) where the prestrain in the top substrate ε_{t_sub} relaxes from 50% to 0% (corresponding to prestrain in the bottom substrate ε_{b_sub} from 100% to $(1+\varepsilon_{t\_sub})/(1+\varepsilon_{b\_sub})-1=33\%$), release of the prestrain in the top substrate initiates controlled buckling of the 2D precursor. The relative height of the buckled ribbon structure (represented by h/d) increases following the release of ε_{t_sub}, and reaches a maximum value of approximately 0.4 as the top substrate returns to its initial length before stretching (Shape I; $\varepsilon_{t\_sub}=0\%$). Further release of prestrain in the bottom substrate ε_{b_sub} imparts compressive forces at selected locations at the bonding sites of the bilayer substrate, thereby enabling the top substrate to buckle into a 3D cross structure with relative height H/D. During this stage, the bonding sites of the 2D precursor follow the deformation of the top substrate into a non-planar configuration, while the relative height of the PI ribbon h/d remains almost unchanged. Fully releasing the prestrain in the bottom substrate completes this Stage II assembly where H/D reaches a maximum value of approximately 0.35 (Shape II; $\varepsilon_{b\_sub}=0\%$). This sequential compressive buckling of the 2D precursor and the top substrate yields a hierarchical 3D mesostructure in which the two-level buckled structures can be independently controlled by the assembly process. FEA provides accurate predictions of the geometric configuration of the resulting hierarchical 3D structure as indicated by the solid lines in Figure 1a. Experimental results of the intermediate and final geometries exhibit quantitative agreement with FEA, showing clearly the two distinct stages of the assembly process. Some small discrepancies may originate from imperfections of the patterned structures and bonding between them.

2.2. Influence of Geometric Parameters and Substrate Prestrain

For the basic design illustrated in Figure 1a, the dimensions of the 2D precursors and bilayered substrate, the levels of prestrain and the bonding locations affect the buckling mechanics. Figure 1b,c shows the influence of the dimensionless
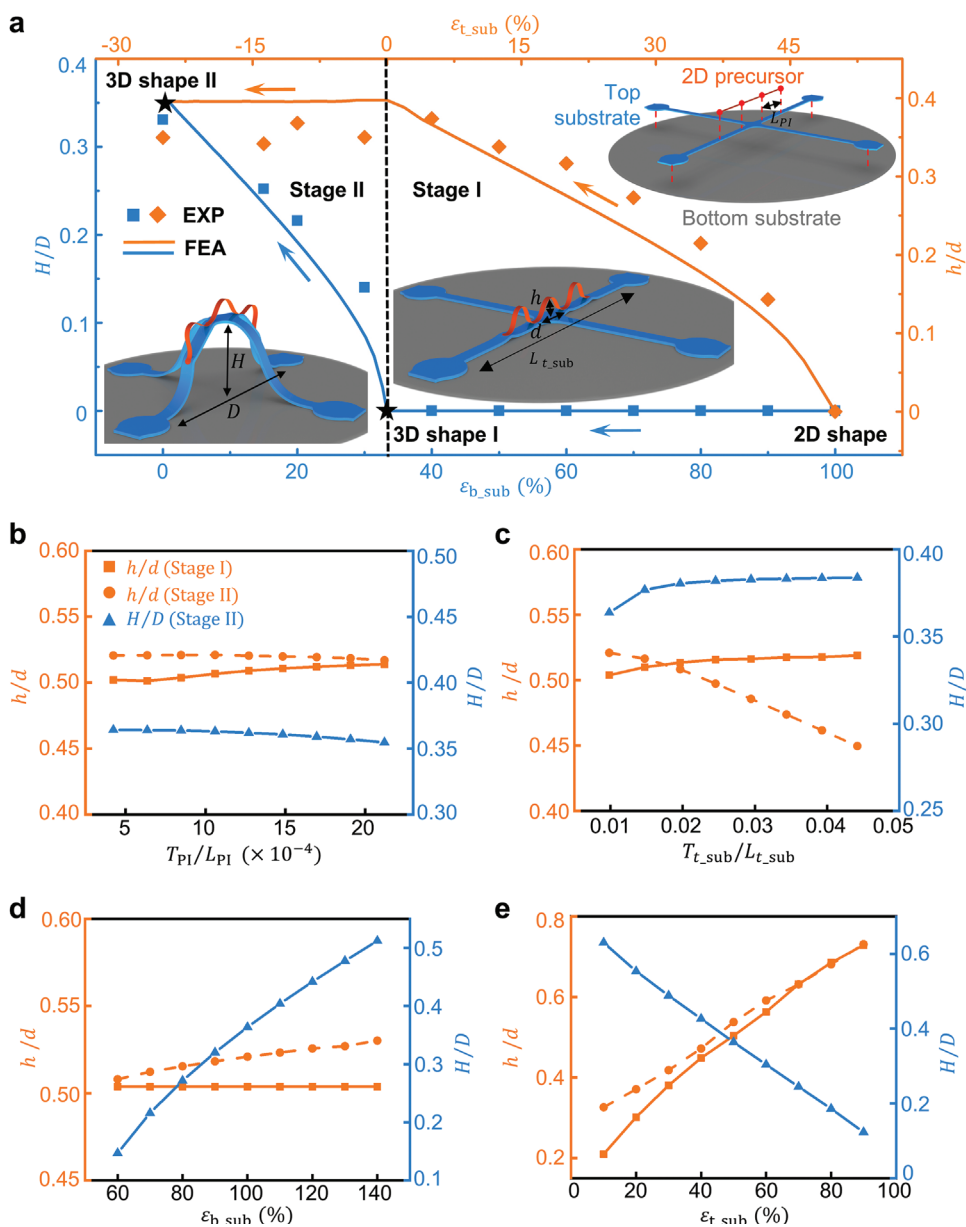
Figure 1. A representative set of 3D mesostructures formed by mechanically guided hierarchical assembly and dependence of their geometries on various design parameters. a) Comparison of FEA and experimental results for a hierarchical 3D arc-shaped ribbon on a 3D cross structure from a two-stage (Stage I and Stage II), sequential compressive buckling process. Orange and blue represent the dimensionless heights of the 3D ribbon and the 3D cross, respectively. Lines and symbols correspond to FEA and experimental results, respectively. b–e) Effects of various design parameters on the dimensionless heights of the 3D ribbon (h/d) and the 3D cross (H/D) in two shapes (Shape I and II) of the hierarchical assembly, including the (b) dimensionless PI thickness (T_{PI}/L_{PI}), (c) dimensionless thickness (T_{t_sub}/L_{t_sub}) of the top substrate, (d) prestrain (ε_{b_sub}) of the bottom substrate, and (e) the prestrain (ε_{t_sub}) of the top substrate.

thicknesses of the PI ribbon and the top substrate (T_{PI}/L_{PI} and T_{t_sub}/L_{t_sub}) on the dimensionless buckled heights (h/d and H/D) of the resulting 3D structures. T_{PI} and T_{t_sub} are the thicknesses of the PI ribbon and the top substrate, respectively; L_{PI} and L_{t_sub} are the length between two adjacent bonding sites on the PI ribbon and the length between the bonding sites on the top substrate before assembly, respectively (Figure 1a). The dimensionless buckled heights of the PI ribbon in Shape I (h/d) and the top substrate in Shape II (H/D) exhibit negligible changes as the thicknesses of the PI and the top substrate

increase. This behavior follows from the relatively slender geometric features of the 3D PI ribbons compared to those of the top substrate (i.e., $T_{PI}/L_{PI} = 8.5 \times 10^{-4} \ll T_{t\_sub}/L_{t\_sub} = 0.01$). During Stage II, reaction forces applied by the 3D PI ribbons and constraints of the bonding sites influence the local deformations of the top substrate, leading to a segmental deformation mode in the top substrate for $T_{PI}/L_{PI} = 4.2 \times 10^{-4}$ as compared to a smooth profile without the PI ribbons (Figure S3, Supporting Information). Further increases in T_{PI}/L_{PI} from 4.2×10^{-4} to 2.1×10^{-3} result

in negligible shape changes in the top substrate. With an increase of the dimensionless thicknesses of the top substrate (T_{t_sub}/L_{t_sub}), the distance (d) between bonding sites of the middle arc-shaped PI ribbon increases in Shape II, leading to a decrease of the dimensionless buckled heights of the PI ribbon (Figure 1c).

Figure 1d,e illustrates the influence of the prestrains of the bottom and top substrates (ε_{b_sub} and ε_{t_sub}) on the dimensionless buckled heights, respectively. In Shape II, the compressive strain ($\varepsilon_{c\_b\_sub}$) applied to the top substrate is determined by the prestrains of the bottom and top substrates according to $\varepsilon_{c\_t\_sub} = 1-(1+\varepsilon_{t\_sub})/(1+\varepsilon_{b\_sub})$. Therefore, the dimensionless buckled height (H/D) of the top substrate increases with an increase in ε_{b_sub}, but decreases with an increase in ε_{t_sub}. The compressive strain applied to the PI ribbons depends only on the prestrain of the top substrate, and thereby the dimensionless buckled height (h/d) remains unchanged in Shape I as ε_{b_sub} increases. The final 3D geometries of the PI ribbons (in Shape II) depend on the applied compressive strain and the 3D configuration of the top substrate. By consequence, the buckled height in Shape II can be controlled by adjusting the prestrains in the two layers of the substrate (ε_{b_sub} and ε_{t_sub}). Additional FEA results, summarized in Figure S4, Supporting Information, indicate that h/d and H/D do not depend on the effect of gravity for the range of parameters examined experimentally ($T_{t\_sub}/L_{t\_sub} \geq 0.01$ and $20\% < \varepsilon_{t\_sub} < 80\%$). The effect of gravity becomes significant only when the dimensionless thickness of the top substrate is very small, for example, $T_{t\_sub}/L_{t\_sub} \leq 0.005$.

2.3. Design Strategies

The strategy illustrated in Figure 1a provides access to a variety of hierarchically buckled 3D mesostructures. Design parameters include the shapes of the 2D precursor and the top substrate, arrangements of the bonding sites between them, as well as the prestrains used for both the top and bottom substrates. **Figure 2** shows several examples. The structure in the top panel features a spider net-like 2D precursor with bonding sites on the four branches of a cross-shaped top substrate. Compressive buckling of the 2D precursor occurs not only along each branch, but also between adjacent branches of the cross, to form a complex 3D net mesostructure on the buckled cross-shaped substrate. The middle panel highlights a square mesh 2D precursor and the resulting 3D mesh with the four corners folded downward due to the arrangement of bonding sites on the buckled top substrate. The bottom panel shows a 3D open cage structure on a ring-shaped top substrate, as an example of a different top substrate layout that supports complex arrangements of 2D precursors in 3D space. The agreement between FEA and experiments demonstrated in these examples further validates the use of FEA as an effective design and prediction tool.
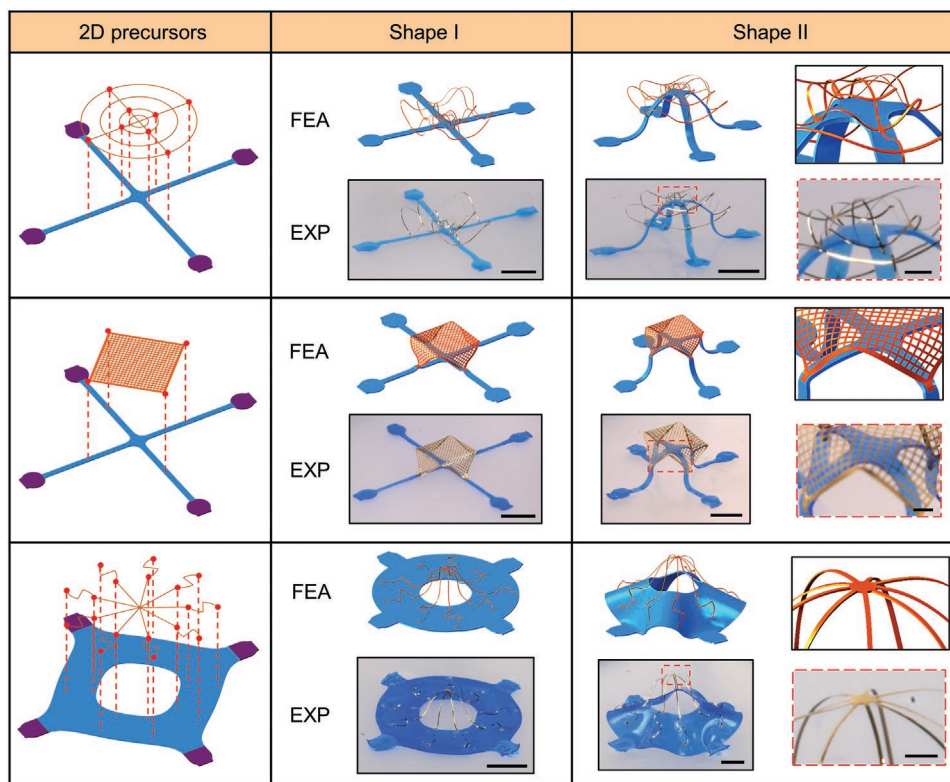
Figure 2. 2D geometries, FEA predictions, and experimental results (optical images) of 3D mesostructures formed by mechanically guided hierarchical assembly featuring designs with 2D precursors bonded to the top substrate. Shape I and Shape II correspond to the shapes formed after the Stage I and Stage II of the assembly, respectively. Red dots represent bonding sites between the 2D precursor and the top substrate, and purple areas represent bonding sites between the top and bottom substrates. The right column in Shape II shows enlarged views of selected regions. Scale bars, 5 mm in solid boxes and 1 mm in dashed boxes.
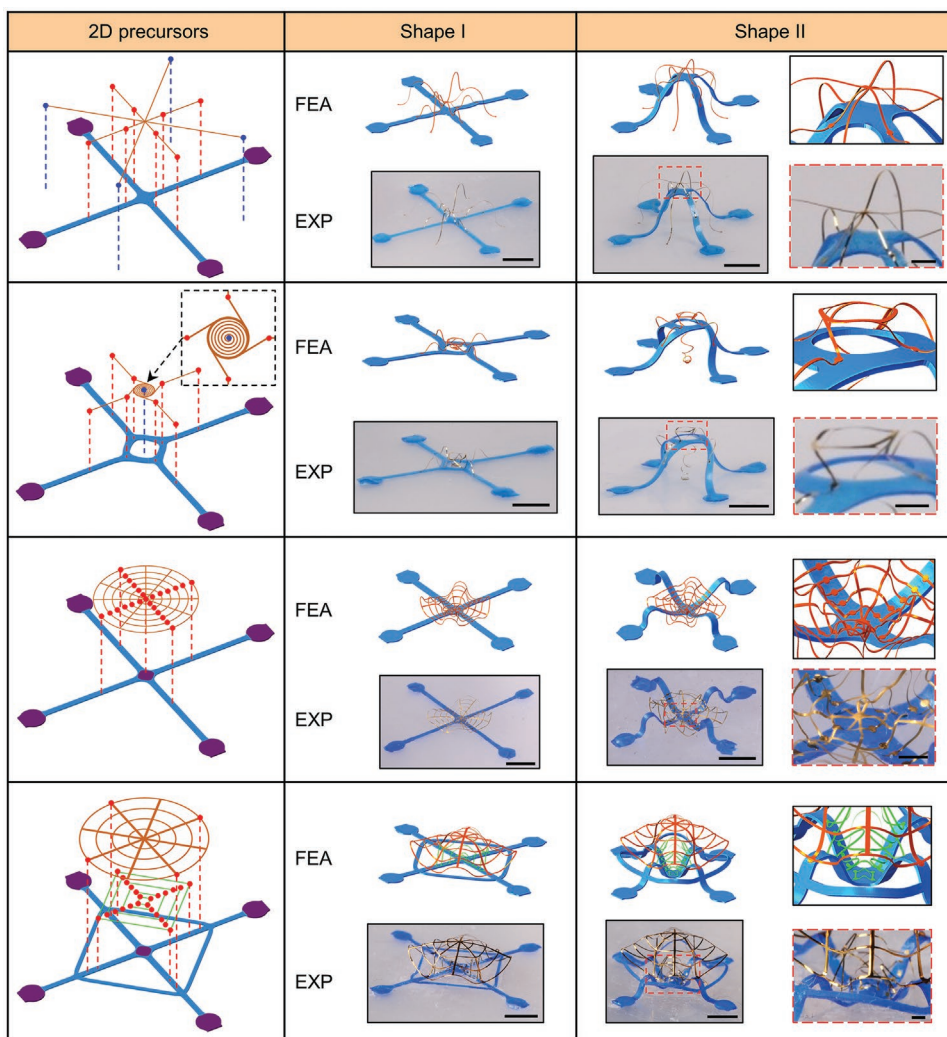
Figure 3. 2D geometries, FEA predictions, and experimental results (optical images) of 3D mesostructures formed by mechanically guided hierarchical assembly featuring designs with 2D precursors bonded to both the top and bottom substrates. Shape I and Shape II correspond to the shapes formed after the Stage I and Stage II of the assembly, respectively. Red and blue dots represent bonding sites between 2D precursors and the top and bottom substrates, respectively. The right column in Shape II shows enlarged views of selected regions. Scale bars, 5 mm in solid boxes and 1 mm in dashed boxes.

Extending the arrangements of bonding sites of the 2D precursor to the bottom substrate increases the types of 3D structures that can be achieved. In the examples presented in **Figure 3**, bonding sites defined on the 2D precursors serve as interfaces to both the top substrate (represented by red dots) and the bottom substrate (represented by blue dots). Such designs distribute the base regions of the 2D precursor across large areas and through the vertical direction, thereby yielding sophisticated geometries that include hierarchical crosses and vertically aligned helices. For instance, the top panel highlights a 2D precursor with short and long ribbons bonded to the top and bottom substrates, respectively. Stage I assembly causes the 2D precursor to form buckled, connected ribbons; Stage II lifts the central portion of the ribbons due to buckling of the cross-shaped top substrate. The 2D precursor in the second panel is a spiral connected with four outer ribbons, where the two ends of each outer ribbon are bonded to the top substrate, and the center of the spiral is bonded to the bottom substrate. Stage I

leads to compressive buckling of the four ends and lifting of the outer circle (Shape I). Stage II triggers buckling of the top substrate into a twisted table with an open hole through which the center of the helix bonds to the bottom substrate, thereby creating a vertically aligned helix across two floors (Shape II).

The arrangement of bonding sites between the top and bottom substrates can also be designed over a broad range of possibilities to give rise to different 3D shapes in the top substrate. For example, adding a bonding site at the center of the basic cross-shaped top substrate changes the resulting 3D shape from convex to concave, as shown in the third panel in Figure 3. This arrangement, when combined with multiple layers of 2D precursors, provides access to spherical nested cages with complex internal structures. The last panel in Figure 3 showcases such an example in which a bilayer (an orange layer above a green layer) of 2D precursors bonds to a top substrate. The top substrate adopts a cross shape with a square frame, where bonding sites between the top and bottom

**ADVANCED
SCIENCE NEWS**

www.advancedsciencenews.com

**ADVANCED
MATERIALS**

www.advmat.de

substrates reside at the ends and the center of the cross. Stage I assembly causes both 2D precursor layers to move upward out of the plane. During Stage II, controlled buckling of the top substrate forms a concave hemispherical cage and folds the green 2D precursor layer inward. The result is a nested cage with buckled ribbons facing the central vertical axis. Figure S5, Supporting Information, shows magnified views of some of the final 3D mesostructures in Figures 2 and 3. Additional examples of 3D mesostructure designs with different 2D precursor/top substrate layouts and bonding site arrangements appear in Figure S6 and Figure S7, Supporting Information. These illustrations include a mesh basket, various combinations of 3D ribbons/membranes spatially located at 3D membranes, and a cage that consists of a top mesh hemisphere and four panels at the bottom.

As demonstrated in Figures 2 and 3, the hierarchical 3D assembly processes introduced here provide access to complex 3D mesostructures that cannot be realized using previously reported approaches. Examples include 3D structures with bonding sites across multiple layers (e.g., the first two mesostructures in Figure 3), as distinct from those formed by buckling of multilayer 2D precursors on a single substrate.[41] Also, the two-stage, reversible assembly process with independently controllable prestrains in different, patternable elastomeric substrates overcomes limitations of a two-level, irreversible buckling process on a single elastomeric substrate in which the buckling of the bottom layer is caused by a partial release of the prestrain in the top buckled layer without independent control of the two-level buckling.[50]

This hierarchical assembly strategy is not limited to forming 3D mesostructures on one side of the bottom substrate; instead, it can also support buckling assembly selectively directed to both sides of the bottom substrate. Figure S8, Supporting Information, presents a 3D mesostructure consisting of multiple ribbons on both sides of the bottom substrate, inspired by designs of 3D multistable structures reported previously.[40,44,45] The bottom substrate is designed with a rectangular hole in the center, and the middle and top substrates are arranged in a cross position. The top, middle, and bottom substrates are prestretched to predefined strain levels ($\varepsilon_{t\_sub\_x} = 50\%$, $\varepsilon_{m\_sub\_y} = 30\%$, and $(\varepsilon_{b\_sub\_x}, \varepsilon_{b\_sub\_y}) = (60\%, 29\%)$), with the bonding sites of the middle substrate close to the edges of the central hole (Figure S8a, Supporting Information). Due to the geometric constraint of the top substrate, the middle substrate is forced to buckle downward through the central hole during the prestrain releasing process. After the first stage of the hierarchical assembly (Stage I), the prestrain in the top substrate is fully released ($\varepsilon_{t\_sub\_x} = 0\%$), while the middle substrate is compressed with a strain level of 19.7%. The top substrate is strategically arranged along the x direction, and the initial length of the top substrate is much larger than the initial width of the hole (length ratio of approximately 8.2). As a result, the top substrate undergoes an upward buckling deformation in the second assembly stage (Stage II). This unique 3D hierarchical configuration (i.e., Shape II) assembled on the hollow elastomeric frame with two opposite buckling directions is significantly different from reported 3D mesostructures with the upward buckling direction only, demonstrating the versatility of this hierarchical assembly strategy.
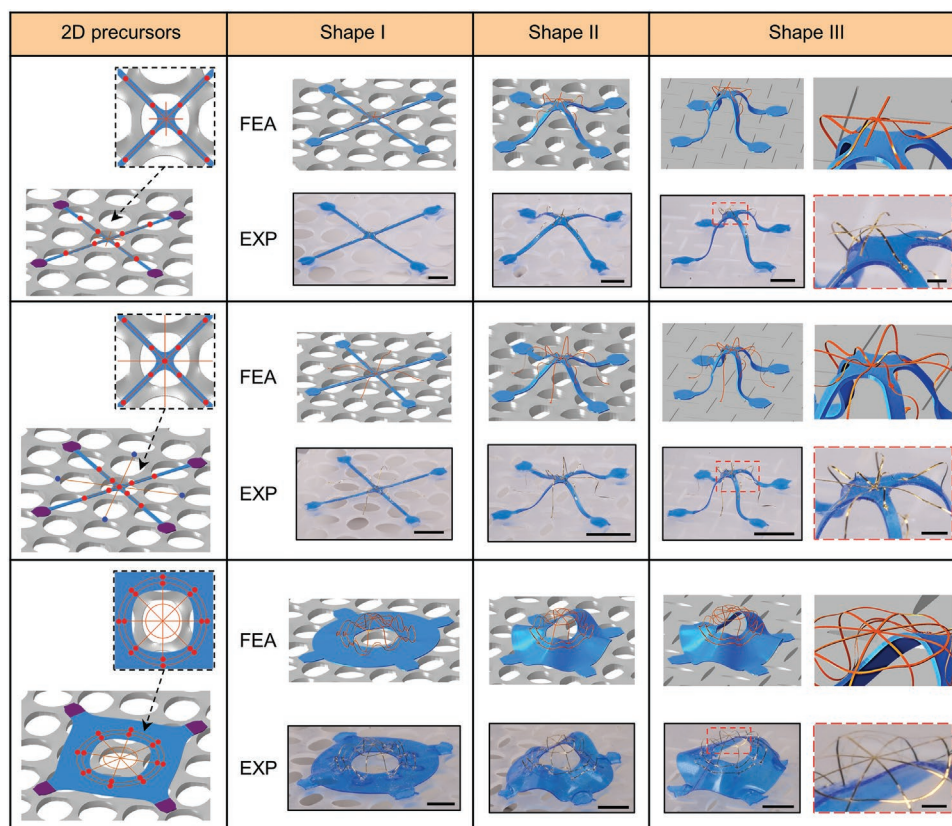
2.4. 3D Mesostructures on Kirigami Substrates

Another class of hierarchical assembly involves non-uniform bottom substrates designed to induce additional deformation patterns in the top substrates. Kirigami substrates, defined as substrates that include engineered cuts, can induce not only translational but also controlled rotational deformations at desired local regions.[44] For instance, a simple kirigami pattern divides the substrate into connected square units using orthogonal cuts. Joining the top substrate and the bottom kirigami substrate involves aligning the bonding sites on the top substrate with designated locations on selected units on the bottom substrate. The use of kirigami bottom substrates divides the compressive buckling of the top substrate into two sub-stages. The first directs transformation of the top substrate into an initial 3D structure by buckling, and the second twists the structure to yield the final shape. In this study, the connected square units have lateral sizes of 8.4 mm, gaps of width 100 µm, and spacings between orthogonal cuts 1.8 mm. For a prestrain of 90% in the bottom substrate, initial relaxation of the prestrain from 90% to 40% releases the stretching of the square units, thereby resulting in compressive buckling of the top substrate. Further relaxation of the bottom substrate leads to rotations of adjacent units in opposite directions due to the release of shear stresses in the individual units (Figure S9, Supporting Information). The maximum rotation angle for the kirigami pattern demonstrated here is approximately 24°. These rotations transform the initial buckled 3D structure into a distinct geometry through twisting. **Figure 4** shows several representative examples of hierarchical assembly designs that incorporate kirigami patterns in the bottom substrates. In these examples, the starting configuration involves a 2D precursor of PI bonded to a top substrate with 40% prestrain, which itself bonds to a kirigami bottom substrate with $\varepsilon_{b\_sub} = 90\%$. Shapes I, II, and III correspond to 3D mesostructures at $\varepsilon_{b\_sub} = 60\%$, 30%, and 0%, respectively. Shape I and Shape II correspond to the sequential, hierarchical assembly process based on the uniform compression-dominated deformation of the top substrate. Further release of the kirigami substrate induces twisting in the top substrate (from Shape II to Shape III), further expanding the 3D shape morphing capability.

The use of kirigami substrates opens access to 3D shapes of the top substrate with chiral characteristics, as demonstrated previously in non-hierarchical cases. In addition to the fractal square cut pattern demonstrated here, other kirigami patterns such as triangle units[51,52] or rectangular units[53,54] provide routes to additional types of twisting patterns applied through the bonding sites of the top substrate.

2.5. Origami-Inspired and Freestanding Structures

Introducing spatial variations in the thicknesses of the 2D precursors can induce the formation of folds at engineered locations during the buckling process, as demonstrated previously in non-hierarchical systems.[39] Due to the cubic downscaling of the bending stiffness with thickness, local reductions in the thickness facilitate folding deformations at those locations. This strategy allows for a diverse range of origami-inspired
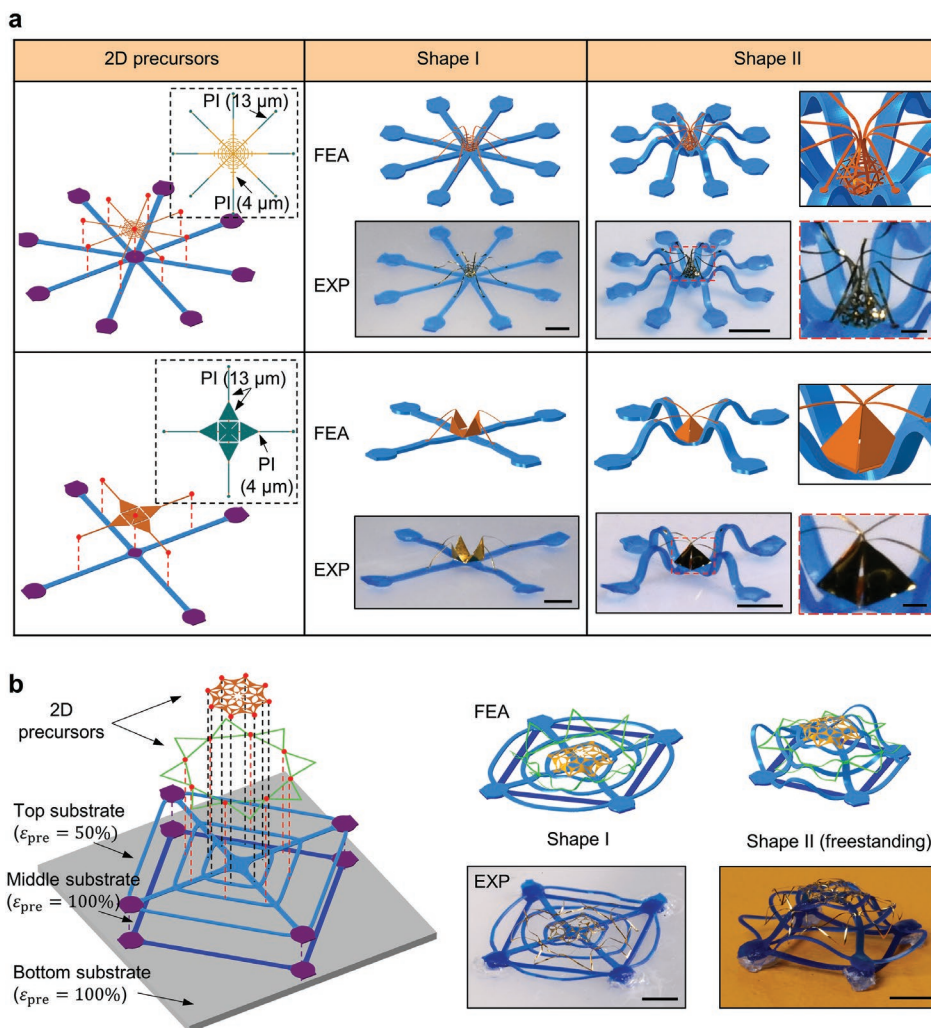
Figure 4. 3D mesostructures formed by mechanically guided hierarchical assembly featuring designs with the top elastomeric substrate bonded on a kirigami bottom substrate. Shapes I, II, and III correspond to the 3D mesostructures at ε_{b_sub} = 60%, 30%, and 0%, respectively. The right column in Shape III shows enlarged views of selected regions. Scale bars, 5 mm in solid boxes and 1 mm in dashed boxes.

geometries including cubic boxes, pyramids, soccer balls, and multi-floor textured buildings.[39,44] The hierarchical assembly scheme introduced in this study provides additional options in folding as a result of compressive buckling of the top substrate. For 2D precursor designs that involve foldable structures bonded to the top substrate, compressive buckling of the top substrate during Stage II of the hierarchical assembly process can induce further folding of the initially buckled 3D structures. **Figure 5**a presents two examples of closed cages that form due to these mechanisms. The 2D precursors consist of PI ribbons or membranes patterned in geometries that have two thicknesses, 4 and 13 µm, corresponding to a bending stiffness ratio of ≈1:34. The fabrication procedures appear in Figure S10, Supporting Information, and the Experimental Section. The structure in the top panel features an open net structure (smallest ribbon width: 100 µm) in the middle (4 µm in thickness) connected with eight ribbons (13 µm in thickness) that act as rigid supports to the net. Stage I assembly yields a half-open, spherical shape due to compressive buckling of the net region supported by eight ribbons. These supporting ribbons remain largely flat in the thick regions owing to the relatively large bending stiffness. Stage II assembly buckles the top substrate further to fold the supporting ribbons towards the center, thereby closing the top half of the net to form a closed cage. Figure S11a, Supporting Information, shows magnified views of the final 3D mesostructure. Quantitative comparisons

of the two origami-inspired 3D shapes in FEA and experimental results appear in Figure S12, Supporting Information, represented by four selected groups of geometric parameters: dimensionless buckled heights of the PI supporting ribbons (h/d) and the elastomeric ribbons in the top substrate (H/D), tilt angle of the PI supporting ribbons away from the horizontal plane (α), and dimensionless distance between the peaks of two opposite supporting ribbons (l/L_{2D}). L_{2D} is the distance between the bonding sites at the two ends of two opposite supporting ribbons on the 2D precursors prior to buckling. The increase in α and decrease in l/L_{2D} in Stage II assembly highlight folding of the supporting ribbons caused by buckling of the top substrate. Data from experimental measurements agree with FEA results, with slight discrepancies that may result from imperfections in the bonding sites and small misalignments between the 2D precursors and the substrates.

The structure in the bottom panel utilizes a different origami-inspired 2D precursor where a square central panel attaches to four triangular panels through narrow (150 µm) and thin (4 µm in thickness) connections. Four thick triangular panels (13 µm in thickness) are supported by ribbons with narrow and thin connections. Stage I assembly folds the four triangular panels to angles of approximately 90° (Shape I). Stage II assembly further folds the four panels toward the center to create a closed pyramid (Shape II) with an additional folding angle of 35°. This hierarchical assembly process transforms a planar structure to a

**ADVANCED
SCIENCE NEWS**
www.advancedsciencenews.com

**ADVANCED
MATERIALS**
www.advmat.de

Figure 5. 2D geometries, FEA predictions, and experimental images (optical) of a) origami-inspired hierarchical 3D closed cages and b) freestanding 3D flower-like mesostructures formed by mechanically guided hierarchical assembly. Shape I and Shape II correspond to the shapes formed after Stage I and Stage II of the assembly, respectively. The right column in Shape II in (a) shows enlarged views of selected regions. Scale bars, 5 mm in solid boxes and 1 mm in dashed boxes.

half-open cage, and then to a fully closed cage. Magnified views of the resultant 3D cage appear in Figure S11b, Supporting Information. Figure S13, Supporting Information, shows the quantitative geometric changes in FEA and experiments from Shape I to Shape II.

Both geometries are qualitatively different from those that can be achieved with conventional schemes in compressive buckling and multilayer assembly on a single elastomeric substrate reported previously.[41] Figure S14, Supporting Information, compares three different types of 3D assembly processes starting from the same prestrain in the bottom substrates with the 2D precursor design for the 3D cage example. 3D hierarchical assembly based on two substrates leads to the closed cage structure shown in Figure 5a. By contrast, 3D multilayer assembly based on a single substrate cannot support a similar two-stage assembly process, and thus the two PI ribbons cannot be significantly separated, thereby preventing the formation of closed structures. 3D monolayer assembly results in a half-closed cage which is similar to Shape I of the

hierarchical assembly process, likewise unable to fully close. The dimensionless number l/L_{2D} and tilt angle α can quantitatively illustrate some of the key differences of the resulting 3D structures following these three types of assembly processes (Figure S14b, Supporting Information). Specifically, buckling of the top substrate in hierarchical assembly closes the 3D cage, corresponding to significantly reduced l/L_{2D} as compared to the other two processes. Also, hierarchical assembly on two substrates features two distinct stages with no out-of-plane tilting of the supporting ribbons in Stage I and large tilting (α up to 34°) in Stage II.

Since the mechanically guided assembly approach is intrinsically compatible with the most advanced planar microfabrication techniques, collections of electronic device components can be readily integrated into these 3D mesostructures. As a simple example, Figure S15, Supporting Information, shows a microscale inorganic light-emitting diode (μ-ILED) assembled on a 3D transparent conductive ribbon formed by 3D hierarchical assembly. Fabrication of the transparent conductive film follows

from light-induced welding of a silver nanowire (AgNW) network on a polyethylene terephthalate (PET) film (12.7 µm in thickness).[55–57] Details of the fabrication process appear in the Experimental Section. In addition to the 3D ribbon geometry shown in Figure S15, Supporting Information, origami-inspired designs can result in functional, compliant, shape-matched frameworks that can serve as mechanical or bioelectronic interfaces to small-scale biological systems such as organoids, spheroids, and assembloids.[58–60] For example, hierarchical assembly can yield not only curved 3D open baskets capable of supporting small-scale spheroids (Shape I), but also top capping structures as a result of Stage II buckling (Shape II). The resulting systems can provide complete full coverage across spherical shapes, as illustrated by FEA results in Figure S16, Supporting Information. Design versatility of the 2D precursor and top substrate also allows for multiple 3D closed cages that can support two spheroids in close proximity, as the basis for forming a well-controlled assembloid (Figure S17, Supporting Information). The results qualitatively expand the options in 3D integration of bioelectronics with spheroids and engineered assembloids as compliant, multifunctional bioelectronic interfaces.[61] The reversible nature of mechanically guided assembly also facilitates the opening and closing of these 3D frameworks, making them well suited for certain bioengineering applications where reversible manipulations are needed, such as cell capture and release.[62]

This hierarchical assembly approach also supports the formation of 3D mesostructures in freestanding forms, separated from the bottom elastomeric substrates. Adding an additional elastomeric layer between the top and bottom substrates can constrain the deformation of the top substrate after separation from the bottom substrate. Figure 5b shows an example of a freestanding, flower-inspired 3D mesostructure formed in this manner. The 2D precursors consist of two layers of patterned polyimide (4 µm in thickness each) designed to resemble stamens (orange mesh) and petals (green ribbons). A top elastomeric substrate in a spider net-like shape at a prestrain of 50% (sky blue; 200 µm in thickness) and a middle substrate in a rectangular frame at a prestrain of 100% (navy blue; 200 µm in thickness) bond to a uniform bottom substrate (2 mm in thickness) at a prestrain of 100%. Stage I assembly buckles the 2D precursors to form a blooming flower-like shape (Shape I), while Stage II buckles the top elastomeric substrate (Shape II). The middle substrate, now without prestrain, supports the buckled shape of the top substrate after separation of the top and middle substrates from the bottom substrate. This strategy for creating freestanding hierarchical 3D mesostructures extends the range of applications of these structures in areas such as soft robotics[63,64] and radiofrequency antennas.[65,66]

3. Conclusion

In summary, we report a hierarchical assembly approach that exploits multiple layers of independently prestretched elastomeric substrates in a buckling-based mechanically guided assembly process that allows the formation of a wide range of 3D structures. In this scheme, release of the prestrain in these substrates induces sequential compressive buckling of them,

and of 2D precursors bonded to them at selected regions. Different design options in the 2D precursor and substrate layouts, as well as bonding site arrangements on the 2D precursor and the substrates, provide access to complex hierarchical 3D topologies previously inaccessible, from vertically aligned helices that cross two levels in the structures, to half-open and fully closed 3D cages. Nearly two dozen examples presented here illustrate the concepts with quantitative computational modeling as a valid design and prediction tool. While these demonstrations use simple polymeric precursors, the approach is intrinsically compatible with a wide range of advanced materials in uniform or patterned thin films, including fully formed planar devices. The two-level hierarchical assembly scheme naturally extends to additional levels. Future work might involve reducing the dimensions of the 3D structures formed by this approach, integrating these 3D hierarchical architectures with microfluidic channels, or incorporating sensing/actuating capabilities via electronic, optoelectronic, and piezoelectric components.

4. Experimental Section

Preparation of Two Layers of Independently Prestretched Substrates for Hierarchical Assembly: A thin (≈0.2 mm) sheet of silicone elastomer (Dragon Skin, Smooth-On; mixed with blue pigment for visualization) patterned by laser ablation (VLS3.50, Universal Laser Systems) served as the top substrate. A representative pattern included a cross with four bonding sites. Pre-stretching the top substrate to an equal biaxial strain of 50% followed by bonding to a transfer frame fixed the prestretched substrate. A separate sheet (≈2 mm in thickness) of silicone elastomer (Dragon Skin, Smooth-On) served as the bottom substrate. Prestretching the bottom substrate to an equal biaxial strain of 100%, spray-coating a thin layer of material (Ease Release 200, Smooth-On) to reduce adhesion, bonding the top substrate on the transfer frame to the prestretched bottom substrate via application of silicone adhesive (Kwik-Sil, World Precision Instruments) on the bonding sites, and removing the transfer frame completed the preparation process.

Fabrication of 2D Precursors for Hierarchical Assembly of 3D Mesostructures: Preparation of 2D precursors began with spin coating (3000 rpm for 30 s) and curing (180 °C for 2 min) a thin layer of poly(methyl methacrylate) (PMMA) onto a clean glass slide, followed by spin coating and fully curing (260 °C for 1 h) a layer of polyimide (2–5 µm; PI-2545, HD MicroSystems). A bilayer of chromium (Cr, 10 nm) and gold (Au, 100 nm) deposited on the PI layer by electron beam evaporation and patterned by photolithography and wet etching served as a hard mask for oxygen plasma etching of the PI. Immersion in acetone overnight dissolved the underlying PMMA layer, thereby allowing the structures to be retrieved from the glass slide and transferred to a water-soluble tape (polyvinyl alcohol, PVA). Deposition of Ti/SiO_2 (10 nm/50 nm in thickness) via sputtering through a shadow mask onto the back sides of the structures defined the bonding sites.

Hierarchical Assembly of Two-Level 3D Mesostructures: The process began with the preparation of two levels of independently prestretched substrates as described above. Exposing the substrate surfaces and the 2D precursors on PVA tape to ultraviolet (UV)-ozone generated surface hydroxyl groups to facilitate bonding. Laminating the 2D precursors/PVA tape onto the prestretched two layers of substrates and heating (70 °C for 10 min) led to strong bonding at the bonding sites defined on the 2D precursors. Dissolving the PVA with water and releasing the prestrain in the two substrates sequentially transformed the 2D precursors into 3D mesostructures.

Fabrication of 2D Precursors for Origami-Inspired, Hierarchical 3D Closed Cages: The process began by spin coating and curing PMMA (same procedure as described above) and PI (1200 rpm for 60 s, 4 µm in thickness) on a glass slide, followed by patterning a bilayer metal

(Cr/Au, 10 nm/100 nm) as an etch mask. Spin coating a second layer of PI (1000 rpm for 60 s, partially curing the PI and repeating the process, 9 µm in thickness in total) followed by patterning another metal etch mask and subsequent oxygen plasma etching of the PI formed a bilayer PI/Cr/Au with different PI thicknesses. Subsequent steps including transfer of the 2D precursors to a water-soluble tape and defining the bonding sites followed the procedures described above. A top elastomeric substrate of thickness 0.4 mm was used for the hierarchical assembly process.

Hierarchical Assembly of 3D Mesostructures on Kirigami Substrates: Preparation of the kirigami substrate involved creating cuts in a sheet (≈2 mm in thickness) of silicone elastomer (Dragon Skin, Smooth-On) by laser ablation (VLS3.50, Universal Laser Systems). Other steps followed the procedures described above.

Fabrication of 3D Hierarchical Electrodes: The process began with defining the outline of a PET film (12.7 µm in thickness) by laser ablation (PLS4.75, Universal Laser Systems). Spin coating (2000 rpm for 30 s) a thin layer of AgNW solution (2 wt.% in isopropyl alcohol, ACS Materials) onto the patterned PET film through a shadow mask defined the electrode area. Exposing the AgNW-coated PET to a UV LED lamp (365 nm, 100 W) for 60 min welded the AgNWs to form a conductive network. Assembly of a microscale LED (270 × 220 × 50 µm in size, TR2227, Gree) across a gap on the AgNW electrodes using silver epoxy completed the preparation of the 2D precursor. Subsequent hierarchical assembly steps followed the procedures described above. Application of a driving voltage of 5 V through thin metal wires connected to the two ends of the AgNW-coated PET ribbon activated the LED.

Modeling of Mechanically Guided Buckling and Twisting: 3D finite element analyses allowed the prediction of the mechanical deformations and the maximum principal strain distributions of 3D hierarchical mesostructures in the multi-stage 3D assembly processes. Four-node shell elements (S4R) and eight-node solid elements (C3D8R) were used to model 2D precursors and elastomeric substrates, respectively. Refined meshes ensured computational accuracy using commercial software (ABAQUS). A hyper-elastic model following the Mooney–Rivlin law described below,

$$U = C_{10}\left(\bar{I}_1 - 3\right) + C_{01}\left(\bar{I}_2 - 3\right) + \frac{1}{D_1}\left(J^{el} - 1\right)^2 \tag{1}$$

was exploited to capture the properties of the elastomeric substrate material with $E_{substrate} = 116$ kPa, and $v_{substrate} = 0.49$. The effects of gravity on the buckling deformations and 3D configurations of top layer elastomeric substrates were incorporated in the FEA analyses. The other relevant material parameters adopted in ABAQUS were $E_{PI} = 2.5$ GPa, $E_{Au} = 78$ GPa, and $E_{Cr} = 279$ GPa, respectively; the Poisson's ratios were $v_{PI} = 0.34$, $v_{Au} = 0.44$, and $v_{Cr} = 0.21$, respectively.

Supporting Information

Supporting Information is available from the Wiley Online Library or from the author.

Acknowledgements

Conflict of Interest

The authors declare no conflict of interest.

Data Availability Statement

The data that support the findings of this study are available from the corresponding author upon reasonable request.

Keywords

[1] D. Karnaushenko, T. Kang, V. K. Bandari, F. Zhu, O. G. Schmidt, *Adv. Mater.* **2020**, *32*, 1902994.

[2] X. Cheng, Y. Zhang, *Adv. Mater.* **2019**, *31*, 1901895.

[3] F. Xu, W. Lu, Y. Zhu, *ACS Nano* **2011**, *5*, 672.

[4] Z. Rao, Y. Lu, Z. Li, K. Sim, Z. Ma, J. Xiao, C. Yu, *Nat. Electron.* **2021**, *4*, 513.

[5] Y. Yu, J. Guo, L. Sun, X. Zhang, Y. Zhao, *Research* **2019**, *2019*, 6906275.

[6] H. Wang, P. Sun, L. Yin, X. Sheng, *InfoMat* **2020**, *2*, 527.

[7] J. Li, G. Liang, X. Zhu, S. Yang, *Adv. Funct. Mater.* **2012**, *22*, 2980.

[8] G. von Freymann, A. Ledermann, M. Thiel, I. Staude, S. Essig, K. Busch, M. Wegener, *Adv. Funct. Mater.* **2010**, *20*, 1038.

[9] Y. W. Kwon, J. Park, T. Kim, S. H. Kang, H. Kim, J. Shin, S. Jeon, S. W. Hong, *ACS Nano* **2016**, *10*, 4609.

[10] H. Li, H. Liu, M. Sun, Y. Huang, L. Xu, *Adv. Mater.* **2021**, *33*, 2004425.

[11] V. A. Bolaños Quiñones, H. Zhu, A. A. Solovev, Y. Mei, D. H. Gracias, *Adv. Biosyst.* **2018**, *2*, 1800230.

[12] W. Xu, S. K. Paidi, Z. Qin, Q. Huang, C.-H. Yu, J. V. Pagaduan, M. J. Buehler, I. Barman, D. H. Gracias, *Nano Lett.* **2019**, *19*, 1409.

[13] B. Li, H. Tan, S. Anastasova, M. Power, F. Seichepine, G.-Z. Yang, *Biosens. Bioelectron.* **2019**, *123*, 77.

[14] Y. Ling, X. Zhuang, Z. Xu, Y. Xie, X. Zhu, Y. Xu, B. Sun, J. Lin, Y. Zhang, Z. Yan, *ACS Nano* **2018**, *12*, 12456.

[15] F. Li, J. Wang, L. Liu, J. Qu, Y. Li, V. K. Bandari, D. Karnaushenko, C. Becker, M. Faghih, T. Kang, S. Baunack, M. Zhu, F. Zhu, O. G. Schmidt, *Adv. Sci.* **2019**, *6*, 1901051.

[16] Z. Lv, Y. Tang, Z. Zhu, J. Wei, W. Li, H. Xia, Y. Jiang, Z. Liu, Y. Luo, X. Ge, Y. Zhang, R. Wang, W. Zhang, X. J. Loh, X. Chen, *Adv. Mater.* **2018**, *30*, 1805468.

[17] S. Zheng, X. Shi, P. Das, Z.-S. Wu, X. Bao, *Adv. Mater.* **2019**, *31*, 1900583.

[18] M. Kadic, G. W. Milton, M. van Hecke, M. Wegener, *Nat. Rev. Phys.* **2019**, *1*, 198.

[19] S. Babaee, J. Shim, J. C. Weaver, E. R. Chen, N. Patel, K. Bertoldi, *Adv. Mater.* **2013**, *25*, 5044.

[20] E. Boatti, N. Vasios, K. Bertoldi, *Adv. Mater.* **2017**, *29*, 1700360.

[21] T. Chen, M. Pauly, P. M. Reis, *Nature* **2021**, *589*, 386.

**ADVANCED
SCIENCE NEWS**

www.advancedsciencenews.com

**ADVANCED
MATERIALS**

www.advmat.de

[22] D. Yan, J. Chang, H. Zhang, J. Liu, H. Song, Z. Xue, F. Zhang, Y. Zhang, *Nat. Commun.* **2020**, *11*, 1180.

[23] H. S. Kang, J. C. Jolly, H. Cho, A. Kalpattu, X. A. Zhang, S. Yang, *Adv. Mater.* **2021**, *33*, 2005454.

[24] Z. Wu, Y. Chen, D. Mukasa, O. S. Pak, W. Gao, *Chem. Soc. Rev.* **2020**, *49*, 8088.

[25] H. Zhu, B. Xu, Y. Wang, X. Pan, Z. Qu, Y. Mei, *Sci. Robot.* **2021**, *6*, eabe7925.

[26] M. Medina-Sánchez, V. Magdanz, M. Guix, V. M. Fomin, O. G. Schmidt, *Adv. Funct. Mater.* **2018**, *28*, 1707228.

[27] Z. Ren, W. Hu, X. Dong, M. Sitti, *Nat. Commun.* **2019**, *10*, 2703.

[28] W. Hu, G. Z. Lum, M. Mastrangeli, M. Sitti, *Nature* **2018**, *554*, 81.

[29] N. T. Jafferis, E. F. Helbling, M. Karpelson, R. J. Wood, *Nature* **2019**, *570*, 491.

[30] Y. Zhang, F. Zhang, Z. Yan, Q. Ma, X. Li, Y. Huang, J. A. Rogers, *Nat. Rev. Mater.* **2017**, *2*, 17019.

[31] H. Zhao, Y. Lee, M. Han, B. K. Sharma, X. Chen, J.-H. Ahn, J. A. Rogers, *Nano Today* **2020**, *30*, 100825.

[32] Y. Yang, X. Song, X. Li, Z. Chen, C. Zhou, Q. Zhou, Y. Chen, *Adv. Mater.* **2018**, *30*, 1706539.

[33] A. Velasco-Hogan, J. Xu, M. A. Meyers, *Adv. Mater.* **2018**, *30*, 1800940.

[34] S. Xu, Z. Yan, K.-I. Jang, W. Huang, H. Fu, J. Kim, Z. Wei, M. Flavin, J. McCracken, R. Wang, A. Badea, Y. Liu, D. Xiao, G. Zhou, J. Lee, H. U. Chung, H. Cheng, W. Ren, A. Banks, X. Li, U. Paik, R. G. Nuzzo, Y. Huang, Y. Zhang, J. A. Rogers, *Science* **2015**, *347*, 154.

[35] Z. Yan, M. Han, Y. Yang, K. Nan, H. Luan, Y. Luo, Y. Zhang, Y. Huang, J. A. Rogers, *Extreme Mech. Lett.* **2017**, *11*, 96.

[36] Y. Zhang, Z. Yan, K. Nan, D. Xiao, Y. Liu, H. Luan, H. Fu, X. Wang, Q. Yang, J. Wang, W. Ren, H. Si, F. Liu, L. Yang, H. Li, J. Wang, X. Guo, H. Luo, L. Wang, Y. Huang, J. A. Rogers, *Proc. Natl. Acad. Sci. USA* **2015**, *112*, 11757.

[37] Z. Fan, Y. Yang, F. Zhang, Z. Xu, H. Zhao, T. Wang, H. Song, Y. Huang, J. A. Rogers, Y. Zhang, *Adv. Mater.* **2020**, *32*, 1908424.

[38] X. Cheng, F. Zhang, R. Bo, Z. Shen, W. Pang, T. Jin, H. Song, Z. Xue, Y. Zhang, *Adv. Mater.* **2021**, *33*, 2102684.

[39] Z. Yan, F. Zhang, J. Wang, F. Liu, X. Guo, K. Nan, Q. Lin, M. Gao, D. Xiao, Y. Shi, Y. Qiu, H. Luan, J. H. Kim, Y. Wang, H. Luo, M. Han, Y. Huang, Y. Zhang, J. A. Rogers, *Adv. Funct. Mater.* **2016**, *26*, 2629.

[40] X. P. Hao, Z. Xu, C. Y. Li, W. Hong, Q. Zheng, Z. L. Wu, *Adv. Mater.* **2020**, *32*, 2000781.

[41] Z. Yan, F. Zhang, F. Liu, M. Han, D. Ou, Y. Liu, Q. Lin, X. Guo, H. Fu, Z. Xie, M. Gao, Y. Huang, J. Kim, Y. Qiu, K. Nan, J. Kim, P. Gutruf, H. Luo, A. Zhao, K.-C. Hwang, Y. Huang, Y. Zhang, J. A. Rogers, *Sci. Adv.* **2016**, *2*, e1601014.

[42] Y. Park, H. Luan, K. Kwon, S. Zhao, D. Franklin, H. Wang, H. Zhao, W. Bai, J. U. Kim, W. Lu, J.-H. Kim, Y. Huang, Y. Zhang, J. A. Rogers, *Adv. Funct. Mater.* **2019**, *29*, 1903181.

[43] K. Nan, H. Luan, Z. Yan, X. Ning, Y. Wang, A. Wang, J. Wang, M. Han, M. Chang, K. Li, Y. Zhang, W. Huang, Y. Xue, Y. Huang, Y. Zhang, J. A. Rogers, *Adv. Funct. Mater.* **2017**, *27*, 1604281.

[44] H. Zhao, K. Li, M. Han, F. Zhu, A. Vázquez-Guardado, P. Guo, Z. Xie, Y. Park, L. Chen, X. Wang, H. Luan, Y. Yang, H. Wang, C. Liang, Y. Xue, R. D. Schaller, D. Chanda, Y. Huang, Y. Zhang, J. A. Rogers, *Proc. Natl. Acad. Sci. USA* **2019**, *116*, 13239.

[45] H. Fu, K. Nan, W. Bai, W. Huang, K. Bai, L. Lu, C. Zhou, Y. Liu, F. Liu, J. Wang, M. Han, Z. Yan, H. Luan, Y. Zhang, Y. Zhang, J. Zhao, X. Cheng, M. Li, J. W. Lee, Y. Liu, D. Fang, X. Li, Y. Huang, Y. Zhang, J. A. Rogers, *Nat. Mater.* **2018**, *17*, 268.

[46] K. Bai, X. Cheng, Z. Xue, H. Song, L. Sang, F. Zhang, F. Liu, X. Luo, W. Huang, Y. Huang, Y. Zhang, *Sci. Adv.* **2020**, *6*, eabb7417.

[47] G. Luo, H. Fu, X. Cheng, K. Bai, L. Shi, X. He, J. A. Rogers, Y. Huang, Y. Zhang, *J. Mech. Phys. Solids* **2019**, *129*, 261.

[48] W. Pang, X. Cheng, H. Zhao, X. Guo, Z. Ji, G. Li, Y. Liang, Z. Xue, H. Song, F. Zhang, Z. Xu, L. Sang, W. Huang, T. Li, Y. Zhang, *Natl. Sci. Rev.* **2019**, *7*, 342.

[49] S. Wu, L. Yue, X. Jin, X. Sun, C. Zemelka, H. J. Qi, R. Zhao, *Adv. Intell. Syst.* **2021**, *3*, 2100107.

[50] Y. Shi, P. Pei, X. Cheng, Z. Yan, M. Han, Z. Li, C. Gao, J. A. Rogers, Y. Huang, Y. Zhang, *Soft Matter* **2018**, *14*, 8828.

[51] S. Yang, I.-S. Choi, R. D. Kamien, *MRS Bull.* **2016**, *41*, 130.

[52] Y. Tang, Y. Li, Y. Hong, S. Yang, J. Yin, *Proc. Natl. Acad. Sci. USA* **2019**, *116*, 26407.

[53] Y. Tang, G. Lin, L. Han, S. Qiu, S. Yang, J. Yin, *Adv. Mater.* **2015**, *27*, 7181.

[54] Y. Tang, J. Yin, *Extreme Mech. Lett.* **2017**, *12*, 77.

[55] J. H. Park, G.-T. Hwang, S. Kim, J. Seo, H.-J. Park, K. Yu, T.-S. Kim, K. J. Lee, *Adv. Mater.* **2017**, *29*, 1603473.

[56] J. H. Shin, J. H. Park, J. Seo, T. H. Im, J. C. Kim, H. E. Lee, D. H. Kim, K. Y. Woo, H. Y. Jeong, Y.-H. Cho, T.-S. Kim, I.-S. Kang, K. J. Lee, *Adv. Mater.* **2021**, *33*, 2007186.

[57] X. Liang, J. Lu, T. Zhao, X. Yu, Q. Jiang, Y. Hu, P. Zhu, R. Sun, C.-P. Wong, *Adv. Mater. Interfaces* **2019**, *6*, 1801635.

[58] Y. Park, T. S. Chung, J. A. Rogers, *Curr. Opin. Biotechnol.* **2021**, *72*, 1.

[59] H. Ryu, Y. Park, H. Luan, G. Dalgin, K. Jeffris, H.-J. Yoon, T. S. Chung, J. U. Kim, S. S. Kwak, G. Lee, H. Jeong, J. Kim, W. Bai, J. Kim, Y. H. Jung, A. K. Tryba, J. W. Song, Y. Huang, L. H. Philipson, J. D. Finan, J. A. Rogers, *Adv. Mater.* **2021**, *33*, 2100026.

[60] H. Zhao, Y. Kim, H. Wang, X. Ning, C. Xu, J. Suh, M. Han, G. J. Pagan-Diaz, W. Lu, H. Li, W. Bai, O. Aydin, Y. Park, J. Wang, Y. Yao, Y. He, M. T. A. Saif, Y. Huang, R. Bashir, J. A. Rogers, *Proc. Natl. Acad. Sci. USA* **2021**, *118*, e2100077118.

[61] Y. Park, C. K. Franz, H. Ryu, H. Luan, K. Y. Cotton, J. U. Kim, T. S. Chung, S. Zhao, A. Vazquez-Guardado, D. S. Yang, K. Li, R. Avila, J. K. Phillips, M. J. Quezada, H. Jang, S. S. Kwak, S. M. Won, K. Kwon, H. Jeong, A. J. Bandodkar, M. Han, H. Zhao, G. R. Osher, H. Wang, K. Lee, Y. Zhang, Y. Huang, J. D. Finan, J. A. Rogers, *Sci. Adv.* **2021**, *7*, eabf9153.

[62] Q. Jin, Y. Yang, J. A. Jackson, C. Yoon, D. H. Gracias, *Nano Lett.* **2020**, *20*, 5383.

[63] Z. Yan, M. Han, Y. Shi, A. Badea, Y. Yang, A. Kulkarni, E. Hanson, M. E. Kandel, X. Wen, F. Zhang, Y. Luo, Q. Lin, H. Zhang, X. Guo, Y. Huang, K. Nan, S. Jia, A. W. Oraham, M. B. Mevis, J. Lim, X. Guo, M. Gao, W. Ryu, K. J. Yu, B. G. Nicolau, A. Petronico, S. S. Rubakhin, J. Lou, P. M. Ajayan, K. Thornton, et al., *Proc. Natl. Acad. Sci. USA* **2017**, *114*, E9455.

[64] A. Nojoomi, H. Arslan, K. Lee, K. Yum, *Nat. Commun.* **2018**, *9*, 3705.

[65] F. Liu, X. Cheng, F. Zhang, Y. Chen, H. Song, Y. Huang, Y. Zhang, *Adv. Electron. Mater.* **2019**, *5*, 1900256.

[66] W. Huang, J. Zhou, P. J. Froeter, K. Walsh, S. Liu, M. D. Kraman, M. Li, J. A. Michaels, D. J. Sievers, S. Gong, X. Li, *Nat. Electron.* **2018**, *1*, 305.